Radiobiology and Radiation Protection

Abel Zhou

Abstract

This section provides an overview of ionizing radiation exposure and radiation protection using computed tomography (CT). Patients undergoing CT examinations as part of their diagnosis or treatment are exposed to ionizing radiation. A net benefit is justified for patients against potential risks induced by exposure to ionizing radiation. This section contains two main subsections: (1) radiobiology and radiation protection and (2) radiation dose in CT examinations. The first subsection reviews the interactions between ionizing radiation and matter, biological effects of ionizing radiation, causative relationship between radiation exposures and their effects, and radiation protection methods. The second subsection systematically reviews radiation measurements with a special focus on CT dose metrics and discusses their applications and limitations.

Keywords

Deterministic effect · Stochastic effect · Linear no-threshold (LNT) · Radiation protection · CT dose index (CTDI) · $CTDI_{FDA}$ · $CTDI_{100}$ · $CTDI_{W}$ · $CTDI_{vol}$ · Dose-length product (DLP)

A. Zhou (✉)
Department of Medical Radiation Science, Faculty of Health, University of Canberra, Canberra, Australia
e-mail: abel.zhou@canberra.edu.au

1 Radiobiology and Radiation Protection

Ionizing radiation interacts with the tissues of the human body and can lead to cell damages, such as cell death or changes in cell function. Radiobiology is the study of the effects of ionizing radiation on living organisms. Ionizing radiation is named because of its capability to eject an orbiting electron from its atom. Medical X-ray imaging uses high-energy photons to produce diagnostic or guidance information for the management of diseases. The use of X-ray imaging is regulated owing to its potential health risks, which are minimized by radiation professionals while maximizing the benefit of undergoing an X-ray imaging examination.

1.1 Interactions Between Photons and Matter

Radiation, an energy packet traveling in space at the speed of light, is an electromagnetic wave possessing an electric field and a magnetic field. Radiation is commonly known as photons and is measured in electron volts (eV), kiloelectron volts (keV), or megaelectron volts (MeV). The terms radiation, X-rays, and photons are used interchangeably in X-ray imaging. Photons may also be measured in terms of the wavelength by the relationship $\lambda = h \times c \div E_{ph}$. Here, λ is the

S. Chau, C. Hayre (eds.), *Computed Tomography*, https://doi.org/10.1007/978-981-19-9346-6_1

wavelength, h is the Planck constant ($6.62607004 \times 10^{-34}$ m^{2}kg/s or J/s), c is the speed of light in vacuum (2.99792458×10^8 m/s), and E_{ph} is the energy in J. For example, the wavelength of a 124-eV photon is approximately 10 nm. Wavelength measurements of photons are uncommon in X-ray imaging.

Photons with energies above the binding energy of an orbiting electron can eject an electron from its atom. In X-ray imaging, the X-ray beam consists of many polychromatic photons whose energy ranges from approximately 10–150 keV. The minimum and maximum energies depend on the total filtration and tube voltage, respectively. Photons of these energies can interact with tissues through three interaction models: Rayleigh scattering, Compton scattering, and photoelectric absorption. The interactions between photons and matter are also known as attenuation. The probability of each interaction has a coefficient that is available from the NIST (2004). Interaction probabilities depend on several factors: photon energy, tissue composition, density, and thickness. The total mass attenuation coefficients of soft tissue, bone cortical, and brain are illustrated in Fig. 1 for photon energies from 10 to 150 keV.

An X-ray beam traversing through tissues reduces the total number of primary photons along the path. The reduction of primary photons follows the Bouguer (1729)–Lambert (1760)–Beer (1852) exponential attenuation law expressed in Eq. (1), for a homogenous medium and monoenergetic X-ray beams.

$$I_l = I_0 \times e^{\left(-\frac{\mu}{\rho} \times l\right)} \tag{1}$$

where I_l is the number of photons traversing a distance l in the homogeneous medium without interactions, I_0 is the number of monoenergetic photons entering the medium, μ and ρ are the linear attenuation coefficient and density, respectively, of the medium, and e is the Euler's number, an irrational number approximately equal to 2.71828.

1.1.1 Rayleigh Scattering

Rayleigh scattering or coherent scattering occurs when an incident photon is deflected by the electromagnetic field inside an atom. The photon changes its trajectory, and its energy is preserved. The incident photon interacts with the atom and its orbiting electrons as a whole, leading to a change in its direction (Fig. 2). No electrons are ejected, and the atoms are not ionized. Rayleigh scattering dominates in low-energy X-ray photons, such as those used in mammography. When traversing through a 10-cm soft tissue, an X-ray beam of radiation quality RQT 8 (IEC 60627: 2005)–100 kilovoltage peak (kVp), 0.2 mm Cu added filtration, and 6.9 mm Al first half-value layer, will have approximately 10% of photons

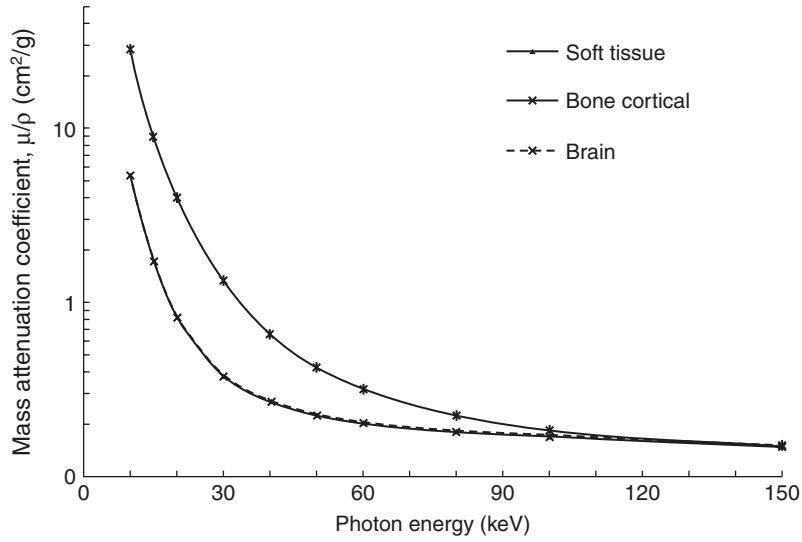

Fig. 1 Total mass attenuation coefficients (μ/ρ) of soft tissue, bone cortical, and brain for photon energies from 10 to 150 keV. μ and ρ are the linear attenuation coefficient and density, respectively

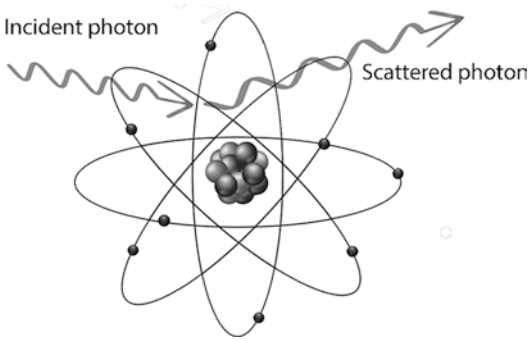

Fig. 2 Rayleigh scattering—the orbiting electrons and the atom interact as a whole with an incident photon and changes its direction without causing energy loss

undergoing Rayleigh scattering, more than 50% undergoing Compton scattering, while approximately 20% undergo photoelectric absorption.

1.1.2 Compton Scattering

Compton scattering, also known as inelastic scattering, was discovered by Arthur Holly Compton. In Compton scattering, an incident photon interacts with an orbiting electron, loses energy, and changes its direction (Fig. 3). A part of the energy of the photon is transferred to the electron, which gains kinetic energy and escapes from the atom. The sum of the kinetic energy and the binding energy of this electron equals the energy lost by the photon. The direction of the electron is confined to an angle that is not more than $\pi/2$ rad with respect to the original direction of the photon. During Compton scattering, photons are more likely to interact with loosely bound or outer-shell electrons. Compton scattering results in scattered radiation and ionization.

1.1.3 Photoelectric Absorption

Photoelectric absorption or the photoelectric effect is the process that an orbiting electron absorbs a photon and escapes from the atom. The electron absorbs all the energy of the photon and escapes from the atom with a kinetic energy equal to the difference between the energy of the photon and the binding energy of the electron (Fig. 4). Photoelectric absorption occurs only if the photon energy exceeds the electron binding energy. A photon is most likely to interact with the electrons

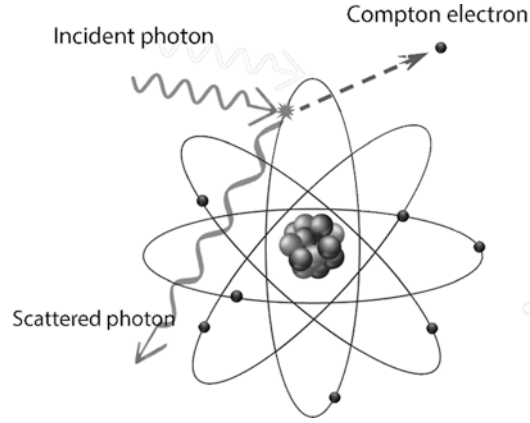

Fig. 3 Illustration of Compton scattering. An incident photon interacts with an orbiting electron. The photon loses some energy and is deflected away from the incident direction. The electron is ejected with a certain kinetic energy

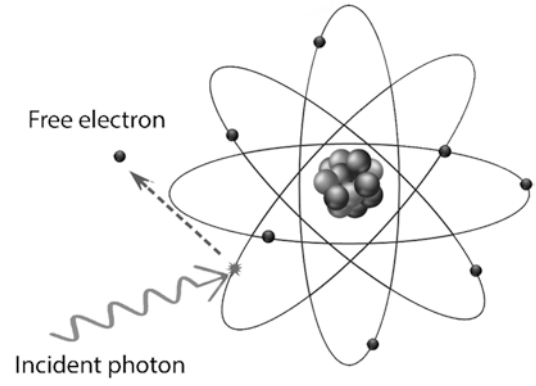

Fig. 4 Illustration of photoelectric absorption. An incident photon is absorbed by an orbiting electron. The electron is ejected with a kinetic energy equal to the difference of the energy of the incident photon energy and the binding energy of the electron

whose binding energies are the closest to, but less than its energy. Photons with energies exceeding the K-shell binding energy are most likely to interact with the K-shell electrons through photoelectric absorption. After a K-shell electron is ejected, the atom is ionized with a K-shell electron vacancy. This vacancy can be filled by an electron from a nearby shell with a lower binding energy (in this example, the L-shell). The electron filling this vacancy, however, can be from any outer shell, for example, the M shell or N shell. As the electron escapes from its orbit, it creates

another vacancy, which is then filled with an electron from an even lower binding energy shell. Thus, an electron cascade from the outer shells to the inner shells occurs. In an electron cascade, the difference in binding energy is released as photons, which are known as characteristic X-rays. A bound electron, possibly from the same shell of the cascading electron, can absorb a characteristic X-ray emitted by the cascading electron. After absorbing the X-ray, this bound electron escapes from the shell and is known as an Auger electron (first discovered by Meitner (1922)). The emission of Auger electrons and characteristic X-rays are competing processes. The probability of the emission of characteristic X-ray decreases as the atomic number of the material decreases. Soft tissues are mostly composed of materials with low atomic number. Characteristic X-ray emission does not frequently occur in soft tissues, but Auger electron emission predominates.

1.1.4 Pair Productions

Photons with energy of at least 1.022 MeV may undergo pair productions with a strong electric field from the nucleus. In a pair production interaction, the photon energy is completely absorbed by the nucleus, resulting in the production of an electron and a positron. The electron and positron have the same energy and are separated by 180° or move in opposite directions.

1.2 Effects of Ionizing Radiation

Interactions between photons and matter result in energy deposition in tissues and damage cells. At the atomic level, these interactions can break chemical bonds, relocate atoms within cell molecules, and lead to change or loss in the function of the molecule and damage cells. Damaged cells may repair themselves correctly and survive. They may incorrectly repair themselves and die. If they survive, they can progress to abnormality or they may not manifest any abnormalities during the lifetime of the person. The effects of ionizing radiation on humans can be deterministic or stochastic.

1.2.1 Deterministic Effects

Deterministic effects include acute damages to the organs and tissues. Damages often occur in the form of the loss of tissue or organ functions, such as cell death and, in extreme cases, death of the irradiated individual. Deterministic effects have threshold doses and occur when the dose exceeds the threshold dose. Some threshold doses are listed in Table 1. Threshold doses depend on the type of irradiated organ/tissue and type of clinical effects on the organ/tissue exposed. If the radiation dose received by an individual exceeds the threshold dose, the severity of the deterministic effect increases as the dose increases. The threshold doses may be revised with an increasing number of observations for deterministic effects. There is much evidence to show that radiation-induced eye cataracts and circulatory diseases occur at lower radiation doses than previous estimations.

1.2.2 Stochastic Effects

Stochastic effects include cancerous and noncancerous risks for irradiated individuals and heritable risks passed on to their offspring. Following

Table 1 Threshold doses for the incidence of morbidity in tissues and organs in adults exposed to acute or chronic irradiation

Effect	Organ/tissue	Time to develop effect	Acute exposure (Gy)	Annual (chronic) dose rate for many years (Gy/year)
Temporary sterility	Testes	3–9 weeks	~0.1	0.4
Permanent sterility	Testes	3 weeks	~6	2.0
Permanent sterility	Ovaries	<1 week	~3	>0.2
Depression of hematopoiesis	Bone marrow	3–7 days	~0.5	>0.4
Cataract (visual impairment)	Eye	>20 years	~0.5	~0.5 divided by years duration

radiation exposures, stochastic effects occur by probabilities, and there is no guarantee that an irradiated individual will develop any signs or symptoms of diseases. There is a latent period before any signs or symptoms manifest. Cancerous risks result from damages to genes by direct or indirect energy depositions in deoxyribonucleic acids (DNAs). Cells have several repair mechanisms that correct themselves during cell division cycles. Unrepaired or wrongly repaired DNA damages may cause cancers in irradiated individuals. These are known as somatic effects. If the damages result in a disease in the offspring of the irradiated individual, it is known as a heritable effect. Heritable risks of radiation exposures are observed among the offspring of Japanese atomic bomb survivors. Non-cancerous risks include cataracts, atherosclerotic diseases, inflammatory responses, and myocardial infarction (Little et al. 2008b; Baker et al. 2011; Picano et al. 2012).

Stochastic effects are proportionally related to the cumulative radiation dose of an individual. The severity of the stochastic effects is not related to the dose. A cancer induced by 2 Gy is not worse than that induced by 0.1 Gy. Stochastic effects have no threshold doses. A single instance of an unrepaired DNA damage can cause cancers or hereditary defects, though with a very low probability (Mossman 2006). The best practice in X-ray imaging involves keeping radiation exposures as low as reasonably achievable (ALARA) to minimize stochastic effects.

1.2.3 Evidence of Ionizing Radiation Effects

On July 31, 2010, the New York Times reported Walt Bogdanich's findings about adverse clinical symptoms including hair loss, headaches, memory loss, and confusion in patients who underwent CT brain perfusion scans because of the intentional use of high levels of radiation to obtain high-quality images. CT brain perfusion scans are performed to evaluate cerebral blood flow, such as in the diagnosis of stroke. More than 400 patients at eight U.S. hospitals might have been affected by brain perfusion scans. These symptoms were due to large acute radiation exposures and are typical examples of deterministic effects.

The stochastic effects of radiation exposure have been observed in a wide range of investigations, such as the increased incidence of cancers in the offspring of Japanese atomic bomb survivors (Little et al. 2009b), development of cancers in experimental animals, and the significantly high rates of cancers among irradiated populations. Significantly higher rates of breast cancers were reported among female patients with tuberculosis who underwent extensive diagnostic fluoroscopy and the incidence was found to be approximately 10–15 years after the initial examinations. Among the patients who received a low dose between 10 and 90 mGy, a significantly higher risk remained (Doody et al. 2000). Higher risks of breast cancers were also reported in patients who underwent radiation therapy for a mean dose of 290 mGy to the breast (Eidemüller et al. 2009, 2011). Similar results were observed in women who were treated for postpartum mastitis with doses typically ranging from 1 to 6 Gy (Hall and Giaccia 2019). An increase in lung cancers has also been reported in patients treated with radiation doses of 5 Gy or more (Travis et al. 2002; Dores et al. 2002). Leukemia is one of the malignant cancers that are most likely linked to radiation exposures. Leukemia is commonly diagnosed in X-ray workers, physicists, and engineers working near accelerators and other sources of ionizing radiation (Little et al. 2009a). The latest evidence of stochastic effects comes from a study of about 950,000 children and young adults (before age 22 years) of nine European countries. The study shows a significantly linear dose-response relationship for brain cancers after CT brain examinations (Hauptmann et al. 2023).

1.3 Linear No-Threshold Model

The risks of cancers owing to exposure to ionizing radiation have been widely observed and are unavoidable. A causative relationship between radiation doses and cancer risks is described by a linear no-threshold (LNT) model that is modeled on epidemiological and animal data (Little et al. 2008a). The LNT theory predicts that stochastic effects are proportional to cumulative radiation

doses. The LNT model is established for high radiation doses with dose-specific estimates of risks determined from people exposed to acute doses of 200 mSv or greater.

In medical imaging, radiation exposure or fractionated exposures with acute fractions are less than a few mSv. It is difficult to detect cancer risks resulting from low radiation doses in epidemiological studies. ICRP (2007) it is generally accepted that the risks from LNT should be divided by the dose and dose-rate effectiveness factor (DDREF) to model the risks at low radiation doses. DDREF values for doses at or below 2 Gy have a value of 2. In comparison, the Biological Effects of Ionization Radiation (BEIR) Committee recommends DDREF values in the range of 1.1–2.3, based on the Bayesian statistics of the combination of the life span studies of atomic-bomb survivors and selected animal studies.

1.4 Radiation Protection

The stochastic effects of radiation exposure are modeled by the LNT theory. The best X-ray imaging practice is to keep radiation exposure ALARA, while producing optimal quality images. The primary goal of radiation protection is to prevent the occurrence of deterministic effects and minimize stochastic effects. In medical X-ray imaging, the principles of justification, optimization, and dose limits are recommended for radiation protection.

The **principle of justification** refers to the fact that every radiation exposure received by patients must be associated with a positive net benefit. The justification principle is intended for healthcare professionals who can prescribe X-ray imaging examinations. It is an effort to reduce radiation exposure to patients by avoiding unnecessary X-ray imaging examinations.

The **principle of optimization** is based on the ALARA principle. This means that all radiation exposures must be kept as low as reasonably achievable without compromising the image diagnostic quality, with economic and social factors taken into consideration. The practical implementation of the ALARA principle requires radiation professionals to apply relevant methods consistently to ensure that the amount of radiation is kept at the minimum while producing images with optimal quality. A practical challenge with the ALARA principle lies in producing acceptable image quality with the lowest possible radiation doses. **Dose limits** are set for regulatory guidance on radiation protection for radiation professionals. It states that the radiation dose a professional receives annually and accumulates over the professional practical period should not exceed the recommended dose limits. These limits are intended to prevent deterministic effects and reduce the stochastic effects of radiation exposure on radiation professionals.

The exposure time, distance from a radiation source, and shielding are essential factors for radiation protection. The total radiation exposure received by an individual is proportional to the exposure time and inverse square of the distance from the radiation source. **Minimizing the time** of exposure to ionizing radiation is an essential method for reducing the total radiation dose received by the individual. Healthcare professionals should minimize the time during which they have to be in areas where the generation of X-rays is active, for example, during CT fluoroscopy examinations. **Increasing the distance** from the radiation source is another important approach for reducing radiation exposure. During X-ray imaging, the radiation from the source is divergent and travels in all directions. The amount of radiation reaching a given area depends on its distance from the source and is proportional to the inverse square of the distance. Thus, the further the source, the less radiation the received. When a patient undergoes a CT examination, the body becomes a source of scattered radiation, which moves in all directions. During CT fluoroscopy examinations, healthcare personnel should stand at a reasonable distance from the scatter source. **The use of shielding** is another effective radiation protection method. Shielding is designed to reduce radiation exposure to personnel. Shielding devices are made of high atomic number materials, such as lead plastics, to absorb radiation. Personal shielding devices commonly include lead aprons, gloves, goggles, and thyroid shielding. Transparent plate-glass shielding

can be used to protect personnel from scattered radiation without limiting vision. The CT room walls are shielded to protect persons from exposure to scattered radiation. Shielding may not be intended for patients; it could not protect the patient from exposure to scattered radiation arising from herself/himself. For the patient, shielding is only useful if it is used to stop the primary beam. If the primary beam must be stopped, beam collimation should first be used to exclude regions where the shielding would have been applied.

1.5 Image Quality Optimization and Dose Reduction

Several techniques are used to reduce radiation exposures to patients and improve image quality. These include beam filtration, collimation, current modulation, automatic exposure control, patient centering, and noise reduction reconstruction algorithms. X-ray beam **filtration** reduces the number of low-energy photons, leading to an increase in the average beam energy. Filtration devices can be applied to deliver radiation in the most appropriate distribution over gantry angles with regard to the regions and shapes of the irradiated anatomy. Beam filtration devices are applied between the X-ray tube and the patient. Some manufacturers have also used filters specific to patient size and/or cardiac CT examinations. **Beam collimation** is applied to limit the beam to the minimal dimensions required. Beam collimation occurs along the *z*-axis to define the body length to be scanned and across the patient table to define a scan field of view (SFOV).

Tube current modulation and **automatic exposure control** (ACE) are used to adjust the radiation exposure in response to variations in imaging object sizes and shapes in real time during data acquisition. Some manufacturers adjust the current based on attenuation changes along the *z*-axis while others control the current by attenuation changes with respect to the gantry rotation (in the *x*–*y* plane). Others combine both approaches to achieve a predetermined image noise level by controlling the current. The application of tube current modulation and AEC is a common radiation dose reduction method found in modern CT scanners.

Patient centering in CT scans, which affects the radiation dose to the patient, is controlled by radiation professionals. Inaccurate centering mostly occurs in the vertical direction (y-axis) owing to too low or high patient table positions and is less frequent for patients lying to the side of the table (x-axis). Occasionally, patients may be off-centered in both directions. Ideal centering requires the patient to be centered on the gantry's iso-center for data acquisition and accurate imaging. Off-centering can lead to partial scan coverage (Fig. 5), increase patient radiation doses, and degrade image quality. With a CT body phantom, a 3-cm off-centering and a 6-cm off-centering resulted in an increase in the patient dose by 18% and 41%, respectively (Li et al. 2007; Toth et al. 2007; Kataria et al. 2016). Off-centering can

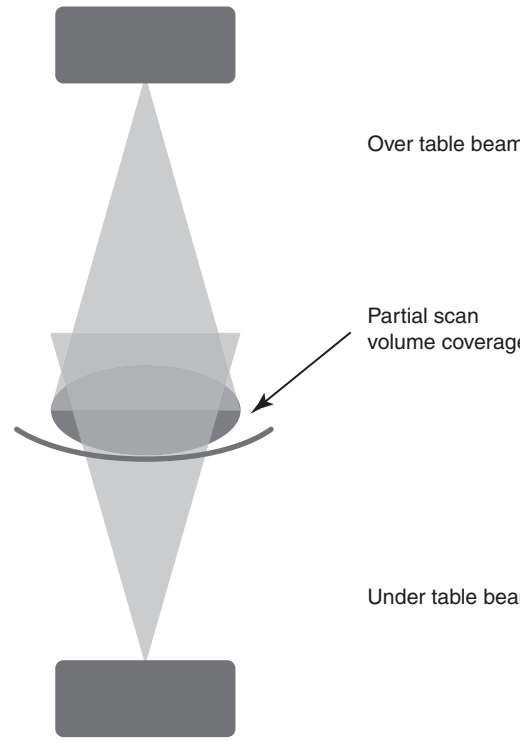

Fig. 5 Illustration of off-centering in the vertical direction. Off-centering can cause partial scan volume coverage, resulting in increased noise and reduced image quality

affect the CT numbers or Hounsfield numbers (HU). CT numbers are converted from linear attenuation coefficients, which are calculated from the sinogram data acquired during the scan. CT numbers are whole numbers truncated from the results calculated using Eq. (2). CT numbers are relative to the linear attenuation coefficient of water. The CT number of water is always zero. Changes of more than 20 HUs were found in a 10-cm off-centering from the iso-center. The majority of off-centering in clinical CT examinations was less than 2 cm and less than 2% of examinations exhibited an off-centering exceeding 4-cm (Szczykutowicz et al. 2017).

$$\mathrm{HU} = 1000 \times \frac{\mu_{\mathrm{tissue}} - \mu_{\mathrm{water}}}{\mu_{\mathrm{water}}} \tag{2}$$

where HU is the Hounsfield number, and μ_{tissue} and μ_{water} are the linear attenuation coefficients of the tissue and water, respectively.

Noise reduction reconstruction algorithms use iterative procedures to reduce image noises. The traditional filtered back projection (FBP) reconstruction method produces high-quality images from data acquired with optimal radiation exposure. For low radiation exposures, the FBPs of most manufacturers fail to reduce image noises and result in poor image quality. Iterative reconstruction (IR) algorithms are generally more useful for image reconstruction at low or ultra-low radiation exposures (Willemink and Noël 2019; Willemink et al. 2014). Many CT manufacturers offer IR algorithms along with their new CT scanners. During the last decade, artificial intelligence (AI) algorithms with the potential for high image quality at ultra-low radiation exposures have emerged for CT image reconstruction. Most IR algorithms fall into two major categories: hybrid and model-based. Hybrid IR algorithms first iteratively filter the sinogram data to achieve noise reduction and then perform back projection. After back projection, the image data are iteratively filtered to reduce image noises. Model-based IR algorithms first perform backward projections to obtain the image data and then perform forward projections to produce artificial sinogram data. The artificial sinogram data are then compared to the real sinogram data, and their differences are used to update the image data. This iteration continues until a predefined condition is reached. A convolutional neural network (CNN) algorithm has shown great success in reducing image noises and the effect of scatter radiation (Zhou et al. 2020). The fundamental advantage of AI is machine learning, in which the algorithm can produce a mapping from raw inputs to specific outputs. CNN algorithms trained with low-dose CT image data have been tested using routine-dose CT images (Wolterink et al. 2017; Chen et al. 2017a,b). AI is expected to play a major role in the reconstruction of CT images. IR algorithms have been proven to be a great technique available in clinical practice for noise reduction.

2 Radiation Dose in CT Examinations

The LNT model quantitatively predicts the causative relationship between cancer risk and radiation exposure. The measurements of radiation delivered to patients are useful for risk assessment in X-ray imaging. The effects of ionizing radiation on tissues depend on several factors, including the amount of energy deposited in the tissue, the type of radiations, and the type of tissues. For the same radiation dose, different types of radiations can have different degrees of effects on tissues. A radiation weighting factor (Table 2) is used to account for the relative biological effectiveness (RBE) of different types of radiations. A tissue weighting factor (Table 3) is used for the radiosensitivity of tissues. Radiation measurements also consider other factors that affect the biological effects. Several radiation measurements are used in X-ray imaging, and some of them are dedicated to CT examinations.

Table 2 Radiation weighting factors

Radiation type	Radiation weighting factor, W_R[#]
Photons, electrons	1
Protons	2
Alpha particles	20
Neutrons (a function of the energy)	5–20

Table 3 Tissue weighting factors

Tissue	W_T, individual	$\sum W_T^{\#}$
Bone red marrow, colon, lung, stomach, breast, remainder tissues[a]	0.12	0.72
Gonads	0.08	0.08
Bladder, esophagus, liver, thyroid	0.04	0.16
Bone surface, brain, salivary glands, skin	0.01	0.04
	Total	1.00

[a]Remaining tissues: adrenals, extrathoracic region, gall bladder, heart, kidneys, lymphatic nodes, muscle, oral mucosa, pancreas, prostate (M), small intestine, spleen, thymus, uterus/cervix (F)

2.1 Absorbed Dose

The amount of energy deposited per unit mass is known as the absorbed dose (Eq. 3), and its SI unit is Gray (Gy) or J/kg. The absorbed dose is one of the most frequently used radiation measurements in X-ray imaging and can be measured with a dosimeter, such as an ionization chamber.

$$D = \frac{\varepsilon}{m} \tag{3}$$

where D is the absorbed dose in Gy (or J/kg), and ε is the energy deposited in a mass of m kg.

2.2 Effective Dose

The effective dose accounts for the biological effects owing to energy deposition, radiation type, and tissue type. To calculate the effective dose, the absorbed dose is ideally measured with a uniform radiation beam exposing the whole body. The effective dose (E) is calculated using Eq. (4), which is the product of the absorbed dose (D), radiation weighting factor (W_R), and tissue weighting factor (W_T).

$$E = W_R \times W_T \times D \tag{4}$$

The effective dose is intended for radiation protection, such as radiation dose assessments for occupationally exposed personnel and planning and optimization in radiological protection. It is a statutory quantity for demonstrating compliance with dose limits and cannot be used to assess individual risks. The effective dose is recommended neither for epidemiological evaluations nor for the detailed specific retrospective investigations of individual exposures and risks.

The application of an effective dose in medical X-ray imaging has limitations. The effective dose facilitates the comparison of biological effects between different types of diagnostic examinations. The effective dose may be used to communicate with patients concerned about the potential harm of their X-ray imaging examinations. The effective dose has an advantage and can be compared to the annual effective dose from naturally occurring background radiation. It varies from region to region and is approximately 3.0 millisievert (mSv) in the United States or 1.5 mSv in Australia.

Controversies over effective dose values may arise because of the calculation methodology and data sources. The effective dose is a measure of the relative "whole-body" uniform radiation exposure, which differs from the exposure to a divergent X-ray beam generated in X-ray imaging. In addition, X-ray imaging examinations often include only a part of the body, variations in the calculation of effective doses for X-ray imaging examinations occur.

2.3 Organ Dose

Organ dose is useful when radiation protection of individual organs is considered. The organ dose is the total energy deposited in an organ divided by its mass. The unit for organ dose is Gy. The direct measurement of organ doses is impractical. They can be appropriately determined using Monte Carlo simulations or experimental setups with phantoms.

2.4 Exposure

Radiation exposure is a measure of the number of electrical charges of a single sign that is produced by ionizing radiation per unit mass of gas, for example, air. Exposure is based on the fact that for each gas, the average energy needed to ionize one pair of ions is constant. For example, the average energy needed to create one pair of ions in air is approximately 34 eV.

Radiation exposure can be directly measured with air-filled radiation detectors for biological purposes because the effective atomic number of the air is close to that of soft tissues. Radiation exposure is nearly proportional to the absorbed dose in soft tissues over the range of photon energies used in medical X-ray imaging. The unit of radiation exposure may be expressed as Roentgen (R) or coulomb per kilogram (C/kg). Exposure can be converted to the absorbed dose. One *R* is approximately 8.73 mGy.

2.5 Dose Distribution in SFOV

Contiguous irradiation during gantry rotations contributes to the radiation dose at a location in the SFOV because of scatter radiation, collimation diaphragms, and geometry of the focal spot. The distributions of radiation doses in the SFOV for small and large imaging objects are illustrated in Figs. 6 and 7, respectively. The radiation doses were higher in the peripheral regions and lower toward the central regions for both the 16-cm diameter head phantom and the 32-cm diameter torso phantom. The distributions also depend on the tube kVp; generally, the lower the kVp, the greater is the difference between the peripheral region doses and the central region doses (Imhof et al. 2003; Geleijns et al. 2009) owing to the greater radiation attenuation of lower energy photons.

2.6 Dose Distribution Along Scan Length

The radiation reaching a location in the SFOV depends on the scattered radiation from the planned scan volume and the geometries of the X-ray focal spot and collimation diaphragms. The radiation dose can be modeled from the radiation distribution of a single-slice scan. In a single-slice scan, an ideal distribution of radiation along the scan length (z-axis) through any point in the SFOV is a square-wave (Fig. 8b) because of the perfect point source (an infinitely

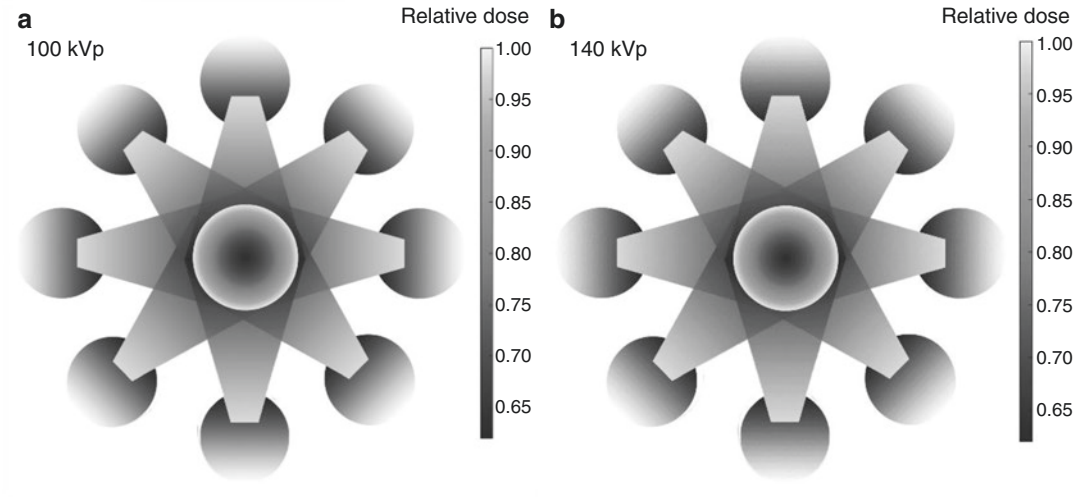

Fig. 6 Radiation dose distributions in a 16-cm diameter head phantom. The doses decrease from the peripheral to the central regions. The doses in the peripheral regions are about 1.5 times the doses in the central areas for both the 100-kVp (**a**) and 140-kVp (**b**). The radiation dose information is from Imhof et al. (2003)

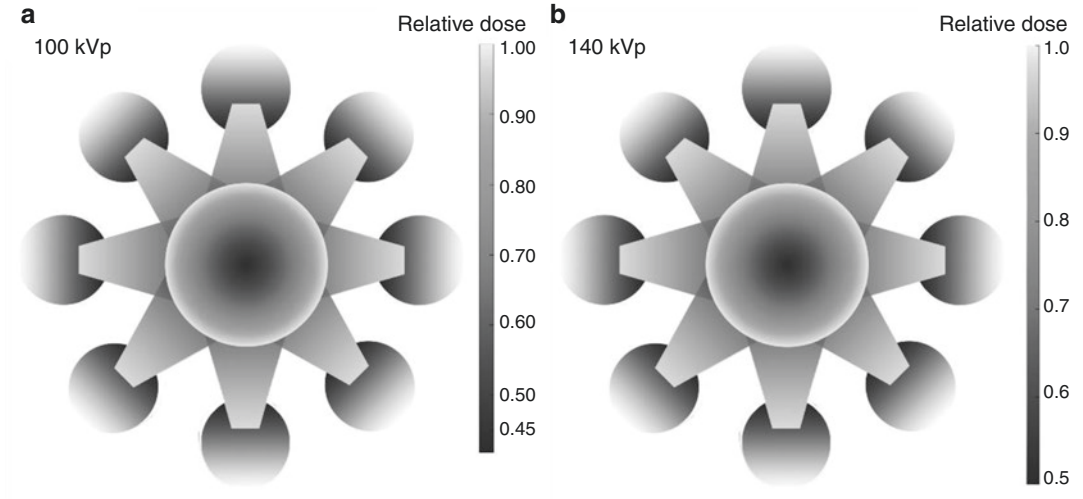

Fig. 7 Radiation dose distribution in a body phantom of 32 cm in diameter with higher doses at the peripheral regions and lower doses at the central region. (**a**): For 100-kVp, the peripheral area doses are about 2.4 times the doses in the central regions. (**b**): For 140-kVp the peripheral doses are about twice the doses in the central regions. The radiation dose information is from Imhof et al. (2003)

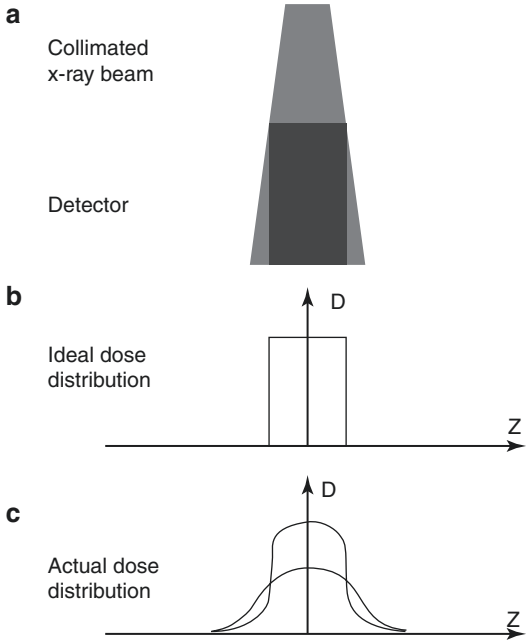

Fig. 8 Distribution of radiation along the scan length (z-axis) from a single-slice scan. (**a**) represents the detector with the collimated x-ray beam source. At any point in the SFOV (the x–y plane), an ideal distribution along the z-axis is a square-wave (**b**). An actual dose distribution closely resembles a narrow bell shape along the z-axis through a point in peripheral regions of the SFOV and broad bell shape along the z-axis through a point in central regions of the SFOV (**c**)

small focal spot) and lack of scattered radiation. The actual radiation distribution is nearly bell-shaped, forming a narrow bell along the scan length through a point in peripheral regions of the SFOV, and a broad bell along the scan length through a point in the central regions of the SFOV (Fig. 8c) (Geleijns et al. 2009).

CT radiation dose assessments are performed under standardized conditions that provide clinical geometries. A small phantom with a diameter of 16 cm and a large phantom with a diameter of 32 cm were used to simulate a patient's head and a torso/body, respectively (Fig. 9). Both phantoms, made from solid acrylic, were drilled with holes at specific locations for placing the pencil dosimeters. When radiation detectors are not placed in the holes, they are plugged using acrylic plugs.

2.7 CT Dose Index

The CT dose index (CTDI) measures the absorbed dose in CT examinations. The CTDI is intended to account for the radiation from a series of adjacent scans by measuring the radiation dose distribution from a single gantry rotation scan. The

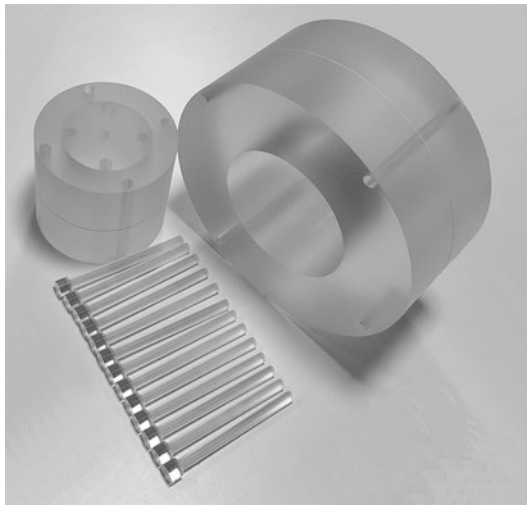

Fig. 9 CT cylindrical acrylic phantom for head and torso radiation dose measurements. The phantom comprised of three cylindrical parts and 13 acrylic plugs which are assembled with an outer diameter of 32 cm for torso dose measurements. The two inner cylinders are assembled with an outer diameter of 16 cm for head dose measurements. The cylinders are 15 cm high with 13 holes drilled through: four holes on the periphery of each cylinder and a central hole on the smallest one

CTDI model is given in Eq. (5). The CTDI is measured in Gy (or J/kg).

$$\mathrm{CTDI} = \frac{1}{nT}\int_{-z}^{z} D(z)\,dz \tag{5}$$

where n is the number of slices acquired in a single gantry revolution (for single-slice scanners, n = 1; for multiple-slice scanners, n depends on the activated data channels used for data acquisition with n = no. of active channels, and one channel is for one image slice). T is the width of a single slice along the z-axis. In single-slice scanners, T is the slice thickness. In multiple-slice scanners, where several detector elements may be grouped together to form one data channel, T is the width of one data channel, and nT is the effective beam width. z is the location along the direction of movement of the patient table. It has a range of values to cover a longer length than the single-slice scan length to measure the radiation dose due to the scan of the multiple slices. $D(z)$ is the dose at location z.The integration in Eq. (5) calculates the area under the dose curve (Fig. 10a).

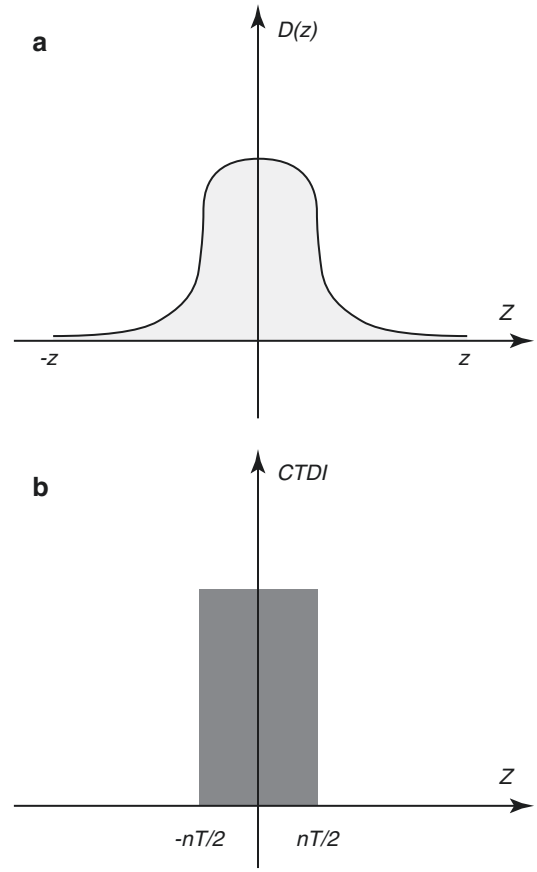

Fig. 10 Illustration of the equivalent area under the curve. (**a**) demonstrates the distribution of the radiation dose along the z-axis resulting from a single-slice scan; (**b**) shows a square-wave CTDI distribution over the X-ray beam width of a single-slice scan. The areas under the curves in (**a**) and (**b**) are equal. (**b**) demonstrates that the CTDI is equivalent to the absorbed dose measured from the radiation that would have only exposed regions given by ($-nT/2$, $nT/2$) but have exposed regions across locations in ($-z$, z)

The physical meaning of this area is the product of dose and length. When the area is divided by the X-ray beam width (nT), it results in an average dose of radiation that would have exposed only regions located in ($-nT/2$, $nT/2$) but had actually exposed regions in ($-z$, z). The average radiation dose within the X-ray beam width (nT) is illustrated in Fig. 10b, in which the area under the CTDI curve equals the area under the dose curve in Fig. 10a. The average radiation dose was calculated using the CTDI. Indeed, the CTDI represents the radiation dose that would have been measured when a series of contiguous irra-

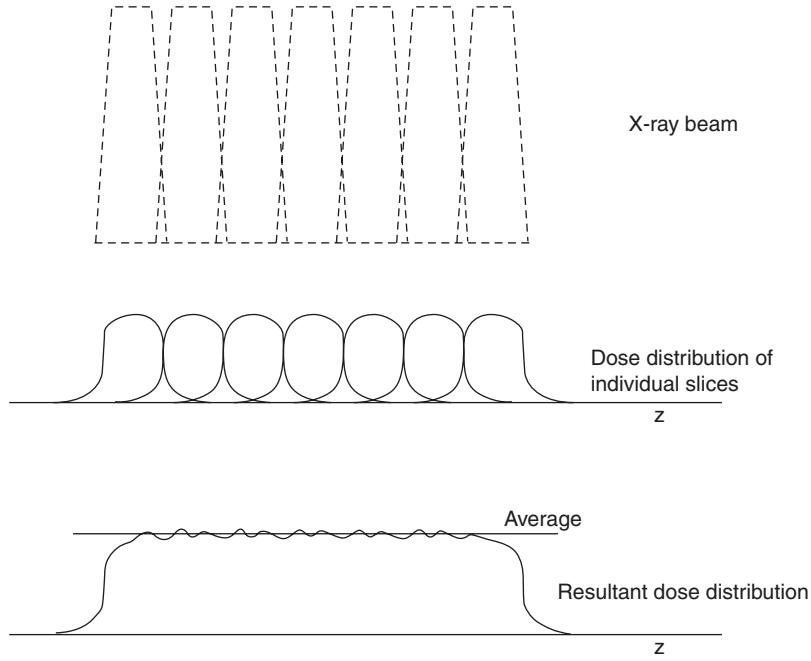

Fig. 11 Illustration of CT radiation dose profile of several contiguous scan slices. Each individual slice has a bell-shaped dose distribution (middle) along the *z*-axis. The resultant dose distribution along the *z*-axis over the range of the scanned slices is shown at the bottom

diations along the z-axis had been performed from $-z$ to z, as illustrated in Fig. 11.

To determine the CTDI, the radiation was measured with a pencil dosimeter from one revolution of the gantry. As the active detection length of the dosimeter is longer than the collimated X-ray beam width (slice thickness), the radiation reaching the adjacent regions is also measured. The result of the measurement using a pencil dosimeter is a dose distribution over the *z*-direction of the scan, or dose versus length along the movement direction of the patient table. The dose distribution is integrated, and the result is then divided by the X-ray beam width (or slice thickness) to obtain an average absorbed dose, the CTDI. The CTDI is determined in the axial scan mode for a single gantry revolution to assess the radiation dose that would have resulted from a series of contiguous irradiations along the z-axis.

2.8 $CTDI_{FDA}$

CTDI does not standardize the width for the integration to include the radiation profile tails, which are illustrated in Figs. 8 and 11. For standardized dose measurements, Food and Drug Administration (FDA) of USA introduced a 14-nominal-slice width to determine the radiation dose, which was then denoted as $CTDI_{FDA}$. $CTDI_{FDA}$ is calculated using Eq. 6 and its unit is Gy. For the determination of $CTDI_{FDA}$, the standard scattering media for the head and torso phantoms are polymethylmethacrylate (PMMA) cylinders with a length of 14-cm cm and diameters of 16 and 32 cm for head and body examinations, respectively.

$$\mathrm{CTDI}_{\mathrm{FDA}} = \frac{1}{nT}\int_{-7T}^{7T} D(z)\,dz, \tag{6}$$

where n is the number of slices acquired in a single gantry revolution (for single-slice scanners, $n = 1$; for multiple-slice scanners, n depends on the activated data channels used in the data acquisition with n equal to no. of active channels). In a single-slice scanner, T is the slice thickness, whereas in multiple-slice scanners, several detector elements may be grouped together to form one data channel and T is the width of one data channel.

2.9 $CTDI_{100}$

$CTDI_{FDA}$ also depends on the nominal slice width and tail of the radiation profiles. Potential

variations in dose measurements owing to the scan-slice width are avoided using $CTDI_{100}$, which represents the average radiation dose at the central region of a 100-mm scan. The determination of $CTDI_{100}$ requires that the radiation dose measurements extend 50 mm to each side of the scan location (Eq. 7). The data for determining $CTDI_{100}$ was acquired using a 100-mm long, 3-cc active volume CT pencil ionization chamber and standard CTDI acrylic phantoms. The measurements were performed with a stationary couch.

$$CTDI_{100} = \frac{1}{nT}\int_{-50}^{50} D(z)\,dz \tag{7}$$

where n is the number of slices acquired in a single gantry revolution (for single-slice scanners, $n = 1$; for multiple-slice scanners, n depends on the activated data channels used in the data acquisition with n = no. of active channels). T is measured in mm. In single-slice scanners, T is the slice thickness, whereas in multiple-slice scanners, T is the width of one data channel formed by detector elements grouped together.

2.10 $CTDI_w$

CTDI, $CTDI_{FDA}$, and $CTDI_{100}$ represent the absorbed dose that would have been measured if contiguous scan slices along the z-axis were performed. They vary across the SFOV from the peripheral regions to central areas. To account for radiation dose variations in the SFOV, an average of $CTDI_{100}$ is proposed estimating the absorbed dose across the SFOV. This quantity, denoted by $CTDI_w$, is calculated by Eq. (8). The values 1/3 and 2/3 approximate the relative areas represented by the center and peripheral regions, respectively.

$$CTDI_w = \frac{1}{3}\times CTDI_{100,center} + \frac{2}{3}\times CTDI_{100,edge} \tag{8}$$

where $CTDI_{100,center}$ and $CTDI_{100,edge}$ are the $CTDI_{100}$ at the central and peripheral areas of the SFOV, respectively.

2.11 $CTDI_{vol}$

The determinations of CTDI, $CTDI_{FDA}$, $CTDI_{100}$, and $CTDI_w$ are performed with a single gantry revolution. Clinical CT scan protocols often cover a range of anatomy and require multiple contiguous gantry rotations to complete data acquisition. The patient table moves a distance equal to, less than, or greater than the collimated X-ray beam width between the gantry rotations. A factor, known as the pitch, is used to describe the ratio of the table movement distance to the beam width. To account for the effect of pitch on the radiation dose, $CTDI_{vol}$, which is calculated using Eq. (9), was used.

$$CTDI_{vol} = \frac{1}{\text{Pitch}}\times CTDI_w \tag{9}$$

where the pitch equals the distance moved by the table in a gantry rotation divided by the beam width. A pitch equal to 1 indicates the absence of a gap between adjacent slices while a pitch less than 1 means an overlap between adjacent slices, and therefore, more radiation exposure to the patient during the scan. A pitch greater than 1 indicates a gap between adjacent slices and hence, less radiation exposure to the patient but compromised image quality.

$CTDI_{vol}$ depends on both the peripheral and central $CTDI_{100}$, which neglects the scatter tails beyond 50 mm on each side of the scan slice. Consequently, this underestimates the equilibrium dose for body scan lengths of 250 mm or more by a factor of 0.6, on the central axis, by about 0.8, on the periphery, and by a factor of 0.7, for the dose-length product for all scan lengths (Boone 2007; Mori et al. 2005).

$CTDI_{vol}$ is a single CT dose parameter that can be measured directly and easily, and represents the average absorbed dose within the scan volume for a standardized phantom. $CTDI_{vol}$ represents the average absorbed dose over the x, y, and z directions for an imaging object whose attenuation is similar to that of the CTDI phantom. $CTDI_{vol}$ neither represents the average absorbed dose for objects of substantially different sizes, shapes, and attenuation, nor measures the total

energy deposited in the scan volume as the scan length is not accounted for by the $CTDI_{vol}$.

2.12 Dose-Length Product

The overall energy deposition in the scan volume given by individual scan protocols can be accounted for by a multiplication factor, known as the scan length. The product of the scan length and $CTDI_{vol}$ is a better approximation to the total energy deposition in the scan volume and is known as the dose-length product (DLP) (Eq. 10), which has a unit Gy·cm.

$$DLP = CTDI_{vol} \times scan\_length \quad (10)$$

DLP indicates the total energy deposited in the scan volume and thus represents the potential biological effect of the examination. This is particularly useful; for example, an abdomen-only CT scan may have a $CTDI_{vol}$ equal to the $CTDI_{vol}$ of an abdomen and pelvis CT examination; the former would have a short scan length and hence a smaller DLP. The difference in these CT examinations shows that DLP is a better approximation of the potential biological effects than $CTDI_{vol}$.

Many contemporary CT scanners take advantage of helical scans, which require data interpolation between two points for all projection angles. Thus, the images at the beginning and end of the helical scan require data acquired beyond the planned scan locations, that is, the beginning and end of the anatomical range that are desired for the scan. This increases the actual scan length at the beginning and end of the helical scan. The increase in DLP owing to the necessary additional scan regions for data interpolation is known as "overranging." In multiple-detector-row CT (MDCT) scanners, the additional scan length strongly depends on the pitch. A typical increase in the scan length is 1.5 times the width of the individual beam. The effect of overranging also depends on the length of the anatomical coverage; the shorter the coverage, the greater the effect.

References

Baker JE, Moulder JE, Hopewell JW. Radiation as a risk factor for cardiovascular disease. Antioxid Redox Signal. 2011;15:1945–56.

Boone JM. The trouble with CTDI 100. Med Phys. 2007;34:1364–71.

Chen H, Zhang Y, Kalra MK. Low-dose CT with a residual encoder-decoder convolutional neural network. IEEE Trans Med Imaging. 2017a;36:2524–35.

Chen H, Zhang Y, Zhang W. Low-dose CT via convolutional neural network. Biomed Opt Express. 2017b;8:679–94.

Doody MM, Lonstein JE, Stovall M, Hacker DG, Luckyanov N, Land CE. Breast cancer mortality after diagnostic radiography: findings from the US scoliosis cohort study. Spine. 2000;25:2052–63.

Dores GM, Metayer C, Curtis RE, Lynch CF, Clarke EA, Glimelius B, STORM H, Pukkala E, van Leeuwen FE, Holowaty EJ, Andersson M, Wiklund T, Joensuu T, Van't Veer MB, Stovall M, Gospodarowicz M, Travis LB. Second malignant neoplasms among long-term survivors of Hodgkin's disease: a population-based evaluation over 25 years. J Clin Oncol. 2002;20:3484–94.

Eidemüller M, Holmberg E, Jacob P, Lundell M, Karlsson P. Breast cancer risk among Swedish hemangioma patients and possible consequences of radiation-induced genomic instability. Mutat Res. 2009;669:48–55.

Eidemüller M, Holmberg E, Jacob P, Lundell M, Karlsson P. Breast cancer risk after radiation treatment at infancy: potential consequences of radiation-induced genomic instability. Radiat Prot Dosim. 2011;143:375–9.

Geleijns J, Salvadó Artells M, de Bruin PW, Matter R, Muramatsu Y, McNitt-Gray MF. Computed tomography dose assessment for a 160 mm wide, 320 detector row, cone beam CT scanner. Phys Med Biol. 2009;54:3141–59.

Hall EJ, Giaccia AJ. Radiobiology for the radiologist. Netherlands: Wolters Kluwer; 2019.

Imhof H, Schibany N, Ba-Ssalamah A, Czerny C, Hojreh A, Kainberger F, Krestan C, Kudler H, Nöbauer I, Nowotny R. Spiral CT and radiation dose. Eur J Radiol. 2003;47:29–37.

International Electrotechnical Commission. Medical diagnostic x-ray equipment-radiation conditions for use in the determination of characteristics. Geneva, Switzerland: International Electrotechnical Commission; 2005.

Kataria B, Sandborg M, Althén JN. Implications of patient centering on organ dose in computed tomography. Radiat Prot Dosim. 2016;169:130–5.

Li J, Toth UK, Seamans TL, Al JE. Automatic patient centering for MDCT: effect on radiation dose. Am J Roentgenol. 2007;188:547–52.

Little MP, Hoel DG, Molitor J, Boice JD, Wakeford R, Muirhead CR. New models for evaluation of radiation-induced lifetime cancer risk and its uncer-

tainty employed in the UNSCEAR 2006 report. Radiat Res. 2008a;169:660–76.

Little MP, Tawn EJ, Tzoulaki I, Wakeford R, Hildebrandt G, Paris F, Tapio S, Elliott P. A systematic review of epidemiological associations between low and moderate doses of ionizing radiation and late cardiovascular effects, and their possible mechanisms. Radiat Res. 2008b;169:99–109.

Little MP, Wakeford R, Kendall GM. Updated estimates of the proportion of childhood leukaemia incidence in Great Britain that may be caused by natural background ionising radiation. J Radiol Prot. 2009a;29:467.

Little MP, Wakeford R, Tawn EJ, Bouffler SD, de Gonzalez AB. Risks associated with low doses and low dose rates of ionizing radiation: why linearity may be (almost) the best we can do. Radiology. 2009b;251:6–12.

Meitner L. Über die Entstehung der β-Strahl-Spektren radioaktiver Substanzen. Z Phys. 1922;9:131–44.

Mori S, Endo M, Nishizawa K, Tsunoo T, Aoyama T, Fujiwara H, Murase K. Enlarged longitudinal dose profiles in cone-beam CT and the need for modified dosimetry. Med Phys. 2005;32:1061–9.

Mossman KL. Radiation risks in perspective. CRC Press; 2006.

NIST. 2004. XCOM: Photon Cross Sections Database [Online]. Available: https://www.nist.gov/pml/xcom-photoncross-sections-database [Accessed 16 Jan 2021].

Picano E, Vano E, Domenici L, Bottai M, Thierry-Chef I. Cancer and non-cancer brain and eye effects of chronic low-dose ionizing radiation exposure. BMC Cancer. 2012;12:157.

Szczykutowicz TP, Duplissis A, Pickhardt PJ. Variation in CT number and image noise uniformity according to patient positioning in MDCT. Am J Roentgenol. 2017;208:1064–72.

The international Commission on Radiological Protection (ICRP) publication 103. Ann ICRP. 2007;37(2.4):2.

Toth T, Ge Z, Daly MP. The influence of patient centering on CT dose and image noise. Med Phys. 2007;34:3093–101.

Travis LB, Gospodarowicz M, Curtis RE, Clarke EA, Andersson M, Glimelius B, Joensuu T, Lynch CF, van Leeuwen FE, Holowaty E. Lung cancer following chemotherapy and radiotherapy for Hodgkin's disease. J Natl Cancer Inst. 2002;94:182–92.

Willemink MJ, Noël PB. The evolution of image reconstruction for CT—from filtered back projection to artificial intelligence. Eur Radiol. 2019;29:2185–95.

Willemink MJ, Takx RA, de Jong PA. Computed tomography radiation dose reduction: effect of different iterative reconstruction algorithms on image quality. Comput Assist Tomogr. 2014;38:815–23.

Wolterink JM, Leiner T, Viergever MA, Isgum I. Generative adversarial networks for noise reduction in low-dose CT. IEEE Trans Med Imaging. 2017;36:2536–45.

Zhou, A., Tan, Q. & Davidson, R. Image enhancement using convolutional neural network. Third International Conference on Image, Video Processing and Artificial Intelligence, 2020 Shanghai, China: SPIE.